# Assessment of Climate Biases in OpenIFS Version 43R3 across Model Horizontal Resolutions and Time Steps

Abhishek Savita[1], Joakim Kjellsson[1,2], Robin Pilch Kedzierski[3,1], Mojib Latif[1,2], Tabea Rahm[1,2], Sebastian Wahl[1] and Wonsun Park[4,5]

[1]GEOMAR Helmholtz Centre for Ocean Research Kiel, Kiel, Germany
[2]Faculty of Mathematics and Natural Sciences, Christian Albrechts University of Kiel, Kiel, Germany
[3]Meteorological Institute, Universität Hamburg, Hamburg, Germany
[4]Center for Climate Physics, Institute for Basic Science (IBS), Busan, Republic of Korea
[5]Department of Climate System, Pusan National University, Busan, Republic of Korea

*Correspondence to*: Abhishek Savita (asavita@geomar.de)

**Abstract.**

We examine the impact of horizontal resolution and model time step on climate of the OpenIFS version 43R3 atmosphere general circulation model. A series of simulations for the period 1979-2019 are conducted with various horizontal resolutions (i.e., ~100, ~50, and ~25 km) while maintaining the same time step (i.e., 15 minutes) and using different time steps (i.e., 60, 30 and 15 minutes) at 100 km horizontal resolution. We find that the surface zonal wind bias reduces significantly over certain regions such as the Southern Ocean, the Northern Hemisphere mid-latitudes, and in tropical and subtropical regions at high horizontal resolution (i.e., ~25 km). Similar improvement is evident too when using a coarse resolution model (~100 km) with a smaller time step (i.e., 30 and 15 minutes). We also find improvements in Rossby wave amplitude and phase speed as well as weather regime patterns when a smaller time step or higher horizontal resolution is used. The improvement in the wind bias when using the shorter time step is mostly due to an increase in shallow and mid-level convection that enhances vertical mixing in the lower troposphere. The enhanced mixing allows frictional effects to influence a deeper layer and reduces wind and wind speed throughout the troposphere. However, precipitation biases generally increase with higher horizontal resolution or smaller time step, whereas the surface-air temperature bias exhibits a small improvement over North America and the Eastern Eurasian continent. We argue that the bias improvement in the highest horizontal resolution (i.e., ~25 km) configuration benefits from a combination of both the enhanced horizontal resolution and the shorter time step. In summary, we demonstrate that by reducing the time step in the OpenIFS model, one can alleviate some climate biases at a lower cost than by increasing the horizontal resolution.

35

## 1. Introduction

37 In the last few decades, Atmospheric-Ocean General Circulation Model (AOGCM) simulations from the Coupled Model

38 Intercomparison Project (CMIP) are widely used to study the internal climate variability and the climate response to external

39 forcing such as increasing atmospheric greenhouse gas concentrations causing global warming. These simulations, however,

40 suffer from long-standing biases **(Bayr et al., 2018; Flato et al., 2014; Gates et al., 1999; Kim et al., 2014; Zhou et al.,**

41 **2020**), which leads to significant uncertainties in short-term and long-term climate projections and potential ecosystem impacts

42 **(Athanasiadis et al., 2022; Couldrey et al., 2021; Meehl and Teng, 2014; Meng et al., 2022)**. These biases can arise from

43 a variety of sources, including inaccurate representation of physical processes, poor initialization of model conditions, or

44 inadequate representation of the Earth's topography and land cover.

45

46 Simulations using Atmospheric General Circulation Models (AGCMs) from the Atmosphere Model Intercomparison Project

47 (AMIP), a part of CMIP, are used to study the internal variability of the atmosphere. The AGCMs are less complex than the

48 AOGCMs as the former are constrained by observed Sea Surface Temperature (SST) and Sea Ice Concentration (SIC). Despite

49 being constrained by the observations, the AGCMs also exhibit biases **(e.g., Gates et al., 1999)**, and some of these biases have

50 persisted for over several phases of AMIP **(He and Zhou, 2014)**. The biases in AGCMs are largely due to the fact that many

51 unresolved processes, such as atmospheric convection, precipitation, clouds, cloud-microphysical and aerosol processes,

52 boundary layer processes, and interactions between the land surface and hydrologic processes, have to be included in a

53 parameterized form in the coarse resolution model **(Ma et al., 2022)**. The treatment of unresolved gravity waves and the

54 relatively large model time step also contribute to the biases in AGCMs **(Flato et al., 2014; Gates et al., 1999)**.

55

56 Recently, **Liu et al. (2022)** analyzed AOGCM simulations and reported that increasing the horizontal resolution of the ocean

57 component one can reduce SST and precipitation biases in the equatorial Pacific, whereas increasing the horizontal resolution

58 of the atmospheric component did not have the same effect. However, other studies found that a high-horizontal resolution

59 atmosphere model better simulates the main features of tropical precipitation, tropical atmospheric circulation, and extra-

60 tropical cyclones while moving from 125 km to 40 km horizontal resolution with relatively small improvements for further

61 enhanced horizontal resolution (**Branković and Gregory, 2001; Jung et al., 2012; Williamson et al., 1995).** Similarly,

62 **Roberts et al. (2018)** found that there was not much improvement in the Integrated Forecasting System (IFS) from the

63 European Centre for Medium-Range Weather Forecasting (ECMWF) when moving horizontal resolution from 50 to 25 km.

64

65 **Jung et al. (2012)** and **Roberts et al. (2018)** demonstrated a time step sensitivity in the coarse and high horizontal resolution

66 model simulations using the OpenIFS and IFS model. **Jung et al. (2012)** found that the precipitation and wind biases were

67    reduced at the coarse horizontal resolution when shortening the model time step from 60 to 15 minutes. **Roberts et al. (2018)**

68    did not find such a significant improvement when reducing the model time step from 20 to 15 minutes in their high-resolution

69    (~25 km) configuration. However, both studies did not investigate the model's sensitivity to changes in the model time step in

70    detail.

71

72    In the research community, there is no standard definition for coarse horizontal resolution, as one study considered 200 km as

73    a coarse resolution (~2°) configuration (**Branković and Gregory,** 2001), whereas another study considered 50 km (0.5°) as a

74    coarse resolution (**Roberts et al., 2018**). Likewise, there is no unique rule for setting the model time step dependent on model

75    resolution. Groups using either the IFS or OpenIFS model at horizontal resolutions of ~100 km have used a relatively long

76    time step of 1 hour (**Hazeleger et al., 2012; Kjellsson et al., 2020; Streffing et al., 2022**) or  45 minutes (**Van Noije et al.,**

77    **2021)**, while other groups using the ARPEGE-Climat with a similar dynamical core use 15 minutes (**Voldoire et al., 2019**).

78    The model's horizontal resolution and time steps are rather chosen on what can be afforded computationally, and their relative

79    contributions to biases in the model's climate are not well documented.

80

81    In this study, we systematically investigate the sensitivity of the OpenIFS model version 43r3v2 to the model time step and

82    horizontal resolution. We mostly focus on the surface zonal winds since they play a crucial role for the ocean circulation in

83    the AOGCMs. We also study the representation of the synoptic-scale variability such as Rossby waves and weather regimes.

84    The paper is structured as follows: section 2 describes the model, experimental design, data and methodology; section 3

85    describes the results and section 4 summarizes the conclusions of this work.

86    **2. Model, Experimental design, Data and Methodology**

87    We conducted a series of experiments with the OpenIFS model. The OpenIFS model is derived from the Integrated Forecasting

88    System at the European Centre for Medium-range Weather Forecasting (ECMWF-IFS) cycle 43 release 3 (43r3). The

89    dynamical core is the same as ECMWF-IFS that uses a two-time-level semi-implicit time stepping with semi-Lagrangian

90    advection (**Temperton et al., 2001**) on a reduced Gaussian grid with a hybrid-sigma vertical coordinate (**Simmons and**

91    **Burridge, 1981**). Likewise, the OpenIFS uses the same model physics as the ECMWF-IFS (**cf. Forbes and Tompkins, 2011;**

92    **Hogan and Bozzo, 2018; Tiedtke, 1993**) but does not include the tangent-linear code or 4D-VAR capabilities. Our version,

93    OpenIFS, is similar to cy43r1 used in **Roberts et al., (2018)**, with the main difference being the new radiation scheme, ecRad

94    (**Hogan and Bozzo, 2018**), introduced in cy43r3. Our experiments are run at three different horizontal resolutions: a low-

95    resolution ($T_{co}$95, ~100 km), a medium-resolution ($T_{co}$199, ~50 km), and a high resolution ($T_{co}$399, ~25 km). All the

96    configurations share the same vertical L91 grid. We did not modify any other model parameters when changing the model

97    horizontal resolutions or model time steps, but we note that some parameters such as launch momentum flux for non-orographic

98  gravity waves scales with resolution in the model. We performed 5 experiments in total (**Table 1**). For simplicity, we now

99  refer now OpenIFS as OIFS in the rest of the sections.

100

101  The lower boundary conditions, i.e., SST and SIC, are taken the from Atmospheric Model Intercomparison Project (AMIP)

102  version 1.1.6 **(Eyring et al., 2016; Taylor et al., 2012)**, which are available as monthly means on a 1º×1º horizontal grid. The

103  external forcing is identical to that used in the CMIP6 simulations except for the aerosol and ozone concentrations, which are

104  taken from monthly mean climatology. SST and SIC are interpolated from monthly to daily frequency and from 1º×1º

105  horizontal resolution to the OIFS horizontal grid using bilinear interpolation. All the simulations are run for the period 1979–

106  2019. We extend the simulations beyond the AMIP protocol for 1979-2014 up to 2019 by using SST and SIC from the ERA5

107  reanalysis and the Shared Socioeconomic Pathways 5 (SSP5) emission scenario. Ozone concentrations are taken from monthly

108  photochemical equilibrium state and aerosol concentrations from monthly CAMS climatology of 11 species.

109

110  Amplitude and phase speed of Rossby wave were computed by performing a Fourier decomposition analysis on 300 hPa daily

111  meridional winds. First, we interpolated both ERA5 and OIFS datasets onto a 2.5º × 2.5º grid using bilinear interpolation. We

112  then applied the Fourier decomposition analysis to determine amplitude and position for each Rossby wave number at each

113  latitude as a function of time. The Rossby-wave amplitude and phase speed were computed for the boreal and austral winter

114  seasons respectively using daily values of amplitude and phase speed over the time period 1979–2019. The phase speed is

115  weighed by daily amplitude squared when computing the seasonal averages. The results are presented in wavenumber-latitude

116  diagrams similar to previous studies **(e.g., Pilch Kedzierski et al., 2020; Wolf and Wirth, 2017).** Our wavenumber-latitude

117  analysis is not directly comparable to both studies mentioned above, because we did not apply any high-pass filtering in time

118  before the Fourier decomposition. While the previous literature had similar diagrams with varying measures of wave

119  amplitude, our detailed analysis of phase speed in such a manner is novel in literature to our knowledge.

120

121  The Weather Regime Patterns (WRPs) were calculated using daily 500-hPa geopotential height (z500) anomalies over the

122  Euro-Atlantic region (30°–90 °N, 80 °W–40 °E) for the boreal winter season during the period 1979-2019. The daily z500

123  daily anomalies were computed by subtracting the daily climatology smoothed by a 20-day running mean from the raw z500

124  data. We calculated the first four Empirical Orthogonal Functions (EOFs) from the ERA5 dataset. In the next step, the OIFS-

125  simulated z500 anomalies were projected on the ERA5 EOFs to obtain Pseudo-Principal Components (Pseudo-PCs). We then

126  applied a K-means clustering algorithm to the individual model pseudo-PCs and observation PCs using four clusters. We chose

127  four clusters because these give the most of the significant clustering. Spatial WRPs are obtained by compositing over all daily

128  z500 anomalies for each regime. More information about the methodology can be found in **Fabiano et al. (2020),** section 3.1.

129  In order to evaluate the WRPs simulated by the OIFS across configurations more quantitatively, we have additionally estimated

130  the Pattern Correlation Coefficient (PCC) between the WRPs identified in the model and ERA5.

131

132  We compare the climate of OIFS to observational and reanalysis datasets. Precipitation is validated against the Global

133  Precipitation Climatology Project **(GPCP; Huffman et al., 1997)**, and the surface air temperature (SAT) against the

134  CRUTEM4 **(Harris et al., 2014; Osborn and Jones, 2014).** We have used the ERA5 reanalysis **(Hersbach et al., 2020)** to

135  evaluate 10-meter surface wind as well as the zonal wind at 300 hPa for the Rossby wave analysis. We use z500 from ERA5

136  to validate the OIFS-simulated weather regimes. We also compare our results with the MERRA2 reanalysis **(Gelaro et al.,**

137  **2017)** and find similar results. Therefore, the comparison with MERRA2 is not shown.

138  **3. Results**

139  **3.1 Global and regional surface bias and deriving processes**

140  The annual mean 10m zonal wind (surface wind hereafter) bias during the period 1979–2019 for the different OIFS

141  configurations is shown in **Fig. 1**. We find that the OIFS-LRA-1h configuration has a large surface wind bias over most of the

142  world ocean, with positive biases in the mid-latitudes (the Southern Ocean, North Atlantic and North Pacific) and negative

143  surface wind biases over the tropical oceans (Tropical Pacific, Tropical Indian and Atlantic Ocean) **(Fig. 1b)**. Thus, the OIFS-

144  LRA-1h configuration simulates too strong surface westerly winds (and wind speed) over the mid-latitude oceans, which, if

145  coupled to an ocean model, may cause biases in upper-ocean mixing and oceanic uptake of heat and carbon.

146

147  The surface wind bias in the OIFS-HRA-15m configuration is reduced significantly **(Fig. 1f)** over most of the world ocean

148  compared to the OIFS-LRA-1h configuration **(Fig. 1b)**, indicating that increasing the horizontal resolution from 100 km to 25

149  km and shortening the time step from 1h to 15-min improves the representation of the surface winds. The surface wind bias

150  also significantly reduces everywhere in the OIFS-MRA-15m configuration **(Fig. 1e)** compared to the OIFS-LRA-1h

151  configuration **(Fig. 1b)**. The surface wind bias in OIFS-MRA-15m is larger than that in the OIFS-HRA-15m configuration but

152  smaller than that in the OIFS-LRA-1h configuration. Similar conclusions are obtained by performing Root Mean Square Error

153  (RMSE) analysis, which shows that the OIFS-HRA-15m configuration has the lowest annual and global mean RMSE of

154  surface wind while the OIFS-LRA-1h configuration has the highest RMSE **(Fig. 2a, black line)**. Though we have found a

155  significant improvement in the wind bias in the OIFA-HRA-15m configuration, it is not clear yet whether the improvement is

156  due to the increased horizontal resolution or the shorter time step.

157

158  Surface wind bias is also reduced in both the OIFS-LRA-30m **(Fig. 1c)** and OIFS-LRA-15m **(Fig. 1d)** configurations compared

159  to the OIFS-LRA-1h configuration **(Fig. 1b)**, and the bias improvement is mostly observed at the same places as in the OIFS-

160  HRA-15m configuration **(Fig. 1f)**. The surface-wind bias improvement is similar in the OIFS-LRA-30m and OIFS-LRA-15

161  configurations, except over the North Pacific and Southern Ocean where the OIFS-LRA-15m configuration has a smaller wind

162  bias than the OIFS-LRA-30m configuration. However, we have not seen a big difference between the OIFS-LRA-30m and

163  OIFS-LRA-15 configurations in the global average RMSE analysis **(Fig. 2a)**.

164

165   The surface-wind bias improvement in the OIFS-HRA-15m and OIFS-LRA-15m configurations not only exists in the annual

166   average but also in boreal winter (DJF) and summer (JJA) (**Fig. 2a blue and red lines**, respectively). Our results are consistent

167   with **Jung et al. (2012)**, as they found a reduction in wind bias in the tropical Pacific region when they shortened the time step

168   in their coarse resolution configuration. However, this study and the **Jung et al. (2012)** study are not consistent with that of

169   **Robert et al. (2020)** who did not find much time-step sensitivity. We speculate that in **Robert et al. (2020),** the reduction

170   from 20 to 15 minutes in their high horizontal resolution (25 km) may be too small. Alternatively, the 20-minute time step

171   could be the optimal time step for the 25 km configuration.

172

173   The surface wind bias in the OIFS-HRA-15m and OIFS-LRA-15m configurations looks similar in pattern, but they differ in

174   magnitude. The OIFS-HRA-15m configuration has a smaller bias in the North Pacific, Peru upwelling and Agulhas Bank

175   regions compared to the OIFS-LRA-15m configuration. We hypothesize that the reduction in surface-wind bias in the OIFS-

176   HRA-15m configuration (**Fig. 1f**) compared to the OIFS-LRA-1h configuration (**Fig. 1b**) is a combination of the enhanced

177   horizontal resolution and shorter time step. The improvement in the OIFS-HRA-15m configuration (**Fig. 1f**) compared to the

178   OIFS-LRA-15m configuration (**Fig. 1d**) is due to only the enhanced horizontal resolution as both configurations use the same

179   time step.

180

181   The zonal-wind bias improvement in the OIFS-LRA-15m is further explored using the online zonal wind tendencies from

182   OIFS which are split into dynamics and physics that includes turbulent diffusion, gravity-wave drag and convection:

183

184   $$du/dt = du/dt_{Dyn} + du/dt_{Turb} + du/dt_{Gwd} + du/dt_{Conv} \qquad (1)$$

185

186   where $du/dt_{Dyn}$ is the sum of the tendencies from advection, pressure gradient and Coriolis force, $du/dt_{Turb}$ includes tendencies

187   from surface processes, vertical diffusion and orography drag, $du/dt_{Gwd}$ includes gravity-wave drag and non-orographic drag,

188   and $du/dt_{conv}$ is the tendency from convection. The individual tendencies on the right-hand side of equation (1) are referred to

189   as Dyn, Turb, Gwd and Conv, respectively. They were stored for each model level in the OIFS-LRA-1h and OIFS-LRA-15m

190   configurations. The lowest model level is at 10m height (assuming surface pressure of 1013hPa), so the 10m wind will behave

191   very similarly to the wind at level k=91.

192

193   The averaged zonal wind and zonal wind tendencies over the Southern Ocean (40º S – 60º S and all longitude) in the OIFS-

194   LRA-1h and OIFS-LRA-15m configurations are shown in **Fig. 3a & b,** respectively. The zonal wind tendency (i.e., $du/dt$) in

195   both OIFS-LRA-15m and OIFS-LRA-1h configurations is very small compared to the other processes (**Fig. 3b, black lines**).

196   Conv provides westward acceleration between the 700 and 900 hPa pressure levels and eastward acceleration below, indicating

197   a downward transport of westward momentum. Dyn acts to accelerate the flow eastward from 700 hPa and below, likely via

198 momentum advection, pressure-gradient and Coriolis forces, while Turb has the opposite effect, likely via surface friction and

199 vertical mixing processes. In the OIFS-LRA-15m configuration, we find a similar balance as in the OIFS-LRA-1h, but the

200 westward acceleration above and eastward acceleration below is enhanced by Conv, likely by increased downward momentum

201 transport, in agreement with the increased shallow and mid-level convection (**Fig. 3d**). The vertical momentum mixing by

202 shallow and mid-level convection reduces the vertical wind shear, making the westerly winds more barotropic. As a result, the

203 westerly winds weaken throughout the troposphere and even in the stratosphere (**Fig. 3a**). We note similar changes in the

204 Northern Hemisphere mid-latitudes, suggesting similar mechanisms are acting. Gwd has a negligible role for the winds in the

205 lower stratosphere and the Gwd term does not appear sensitive to model time step (**Fig. 3b, orange lines**).

206

207 **Fig. 3c** shows the zonal average of the zonal wind tendencies at the lowest level of the model, as a function of the latitude. In

208 the OIFS-LRA-1h configuration, Conv and Dyn accelerate the surface westerly wind in the mid-latitudes (~40º N to ~60º N)

209 in both hemispheres, and these westerly winds are partly balanced by Turb (**Fig. 3c, solid lines**). Dyn has a larger contribution

210 to accelerating the surface westerly winds than Conv (**Fig. 3c, solid lines**). However, the Conv contribution is enhanced in the

211 OIFS-LRA-15m configuration, while the Dyn contribution reduces (**Fig. 3c, dashed lines**). We also find that the contribution

212 to slowing the westerly wind is reduced by Turb in the OIFS-LRA-15m configuration (**Fig. 3c, dashed lines**).

213

214 It is also noteworthy that the individual wind tendencies contribute significantly more in the Southern Hemisphere than in the

215 Northern Hemisphere (**Fig. 3c**). In the low latitudes, both Dyn and Conv contribute to accelerating the easterly winds, which

216 is partly balanced by Turb in the OIFS-LRA-1h configuration (**Fig. 3c, solid lines**). There are no discernible changes in Conv,

217 Dyn or Turb from OIFS-LRA-1h to OIFS-LRA-15m, indicating that the tropical surface winds are relatively insensitive to

218 model time step (**Fig. 3c, dashed lines)**.

219

220 The OIFS-HRA-15m also has the lowest SAT RMSE of all model experiments in both annual and seasonal means, although

221 the RMSE difference across the configurations is not significant (**Fig. 2b**). The reduced SAT RMSE in OIFS-HRA-15m

222 configuration is primarily due to the lowered SAT bias over North America and the eastern part of Russia. Compared to the

223 OIFS-LRA-1h, the SAT RMSE decreases with increased horizontal resolution (OIFS-HRA-15m and OIFS-MRA-15m) and

224 shortened time step (OIFS-LRA-30m and OIFS-LRA-15m) (figure not shown).

225

226 The OIFS-LRA-1h experiment exhibits the lowest precipitation RMSE of all experiments, with RMSE increasing with shorter

227 time step (OIFS-LRA-15m) and increased horizontal resolution (OIFS-HRA-15m) for both the annual and boreal winter means

228 (**Fig. 2c, black and blue lines**). The patterns of regional precipitation biases are similar across the configurations in the mid-

229 and high-latitudes, whereas the precipitation biases increase in the tropics at the high horizontal resolution or in the smaller

230 time step configuration (not shown). The results suggest that some of the cloud and/or convection parameters may be dependent

231 on resolution or time step and need retuning for each configuration.

## 3.2 Rossby wave analysis

**Fig. 4** shows the Rossby wave amplitude (gray and black contours) for ERA5 and the individual OIFS simulations for the boreal winter (**Fig. 4A, DJF, Northern Hemisphere; NH)**) and austral winter (**Fig. 4B, JJA, Southern Hemisphere; SH**). The color in **Fig. 4** denotes the wave amplitude bias relative to ERA5 (model – ERA5), normalized by the ERA5 detrended variability expressed by the standard deviation (std). We focus only on those wave numbers and latitudes that have the highest wave amplitude, because these waves explain most of the variability. The region where the wave amplitude is larger than 5 ms$^{-1}$ is termed "core region", which mostly covers the area that is occupied by the thick black contours in **Fig. 4**. In DJF (NH), at north of 70$^o$ N, the Rossby wave numbers k=1 and k=2 have the largest amplitude in ERA5 whereas at the mid-latitudes (30$^o$ N to 60$^o$ N), the wave numbers between about k=3 and k=9 have large amplitude with the largest amplitude amounting to 8 ms$^{-1}$ at about 40$^o$ N for the wave number k=6 (**Fig. 4Aa**). During JJA (SH), the wave amplitude is located in a similar core region (**Fig. 4Ba)** as that in DJF (NH). The amplitude is largest south of 70$^o$ S for the wave numbers k=1 and k=2 whereas at the mid-latitudes (45$^o$ S to 65$^o$ S), the wave numbers between about k=3 to 5 have large amplitude with the largest amplitude amounting to 9 ms$^{-1}$ is found at 57.5$^o$ S for the wave number k=4 (**Fig. 4Ba**).

In DJF (NH) the OIFS-LRA-1h configuration exhibits a positive bias of ~1.5 std in Rossby wave amplitude (i.e., the waves amplitude bias in OIFS-LRA-1h is 50% larger than the variance from ERA-5) in the core region, in particular for wave numbers k=3-8 at latitudes between 25$^o$ N to 45$^o$ N (**Fig. 4Af**). The large wave amplitude biases (~-4 to -2 std) outside of the core region (mostly near the poles for higher wave numbers) in OIFS-LRA-1h are unimportant as these waves have a small amplitude and little effect on variability. Therefore, these biases are not discussed further for other configurations for both hemispheres.

The Rossby wave amplitude biases in the OIFS-HRA-15m configuration are strongly reduced compared to the OIFS-LRA-1h configuration over the core region (**Fig. 4Ab and 4Af**). The Rossby wave amplitude bias reduction in the OIFS-MRA-15m configuration is similar to that in the OIFS-HRA-15m configuration except for the wave number k=7 at 45$^o$ N, where the wave amplitude bias is larger in the OIFS-HRA-15m configuration (**Fig. 4Ab and 4Ac**). The Rossby wave amplitude biases are progressively reduced from the OIFS-LRA-1h configuration to the OIFS-LRA-30m and OIFS-LRA-15m configurations (**Fig. 4Ad-Af**), indicating a sensitivity of model bias to the time step. The wave amplitude bias for wave number k=7 at 45$^o$ N exists in all the configurations, and it is smaller in the OIFS-LRA-15m configuration than in the other configurations. Overall, both OIFS-LRA-15m and OIFS-HRA-15m configurations are able to reproduce the observed Rossby-wave amplitudes in DJF (NH) better than OIFS-LRA-1h.

In JJA (SH), the Rossby wave amplitude bias in the core region is smaller than in DJF (NH) for all the configurations (**Fig. 4A and 4B**). OIFS-LRA-1h exhibits a positive bias of ~1 std in JJA (SH) for the wave number k=2 at latitude between ~50$^o$ S and ~62.5$^o$ S and for wave numbers k=4 to 5 between 30$^o$ S and 40$^o$ S (**Fig. 4Bf**). The OIFS-HRA-15m and OIFS-MRA-15m

265    configurations exhibits biases above ~2 std at wave numbers k> 6 and latitude 50º S to 70°S, which does not exist in the other

266    coarse resolution configurations (**Fig. 4Bb-Bf**), although we note that the absolute amplitudes are very small for these waves

267    and the impact of the biases is negligible.

268

269    We also analyze the phase speed of Rossby waves for ERA5 and across the OIFS' configurations for DJF (NH) and JJA (SH)

270    seasons (**Fig. 5**). In the ERA5 dataset (**Fig. 5Aa**), the Rossby wave phase speed is positive (i.e., eastward moving, solid contour)

271    for wave numbers greater than 2 (i.e., k>2) at most latitudes. The wave numbers k=1 to 2 have a positive wave phase speed

272    from the equator to 55º N and a negative wave phase speed (i.e., westward moving, dashed contours) between 60º N and 80º

273    N in DJF (NH) (**Fig. 5Aa**). The maximum phase speed is found at wave number k=8 at 40º N, while the minimum is found at

274    wave number k=1 at 60º N (**Fig. 5Aa**). In JJA (SH) (**Fig. 5Ba**), the wave phase speeds are mostly positive and large for all the

275    wave numbers and at each latitude, with the maximum phase speed is observed for the wave numbers between k=6 and k=8

276    and latitudes between 40º S and 60º S, and these waves are moving faster than that in DJF (NH).

277

278    The OIFS-LRA-1h configuration suffers from positive phase speed bias for wave numbers k=4 to 8 at latitudes between 42.5º

279    N and 60º N, i.e., waves move faster eastward than in ERA5, and the bias is larger than 1 std. The bias of ~1 std for wave

280    number k = 6 to 8 at 40º N and 60º N is of particular concern as it is near the maximum wave amplitudes in DJF (**Fig. 4Af**).

281    In general, phase speed biases in the OIFS-LRA-1h configuration are strongly reduced as either horizontal resolution is

282    increased or time step is shortened (**Fig. 5Ab-5Af**). In JJA (SH), the OIFS-LRA-1h configuration exhibits a very large (~1.5

283    std) Rossby wave phase speed bias for most of the wave numbers, which is largest for the wave numbers k=3 to 8 between 25º

284    S to 55º S (**Fig. 5Bf**). Large biases can be found between 15º S and 25º S (~2 std) for most of the wave numbers, but the wave

285    activity is low there (**Fig. 4Bf**). The large phase speed biases are strongly reduced in the OIFS-LRA-30m and OIFS-LRA-15m

286    configurations (**Fig. 5Bd-Bf**), indicating a strong sensitivity to the reduced biases in mean winds and wind speeds (Fig. 1).

287    Overall, the Rossby wave speed bias in the OIFS-HRA-15m configuration is smaller than in the OIFS-LRA-1h configuration

288    (**Fig. 5Bb and 5Bf**). However, we note that both the OIFS-MRA-15m and OIFS-HRA-15m configurations exhibit negative

289    biases south of 55º S for wave numbers k= 1 to 5, that is, the eastward moving waves are slower than in the ERA5 (**Fig. 5Bb**).

290

291    The wave phase speed analysis reveals a clear improvement in the representation of the Rossby waves in the boreal winter

292    (i.e., NH) when increasing the horizontal resolution and shortening the model time step compared to OIFS-LRA-1h

293    configuration. In austral winter, however, the representation of Rossby wave amplitudes and phase speeds are the most realistic

294    in OIFS-LRA-15m configuration, with longer time steps introducing too fast phase speeds and higher horizontal resolution

295    introducing too slow phase speeds at wave number less than 6 (i.e., k<6).

296

### 3.3 Weather regimes pattern

We derive the four weather regimes patterns (WRPs) over NH in the Euro-Atlantic region from ERA5. The patterns resemble the positive and negative phases of the North Atlantic Oscillation (NAO+ and NAO–, respectively), Scandinavian blocking (Sc. Blocking), and the North Atlantic ridge (Atl. Ridge) pattern (**Fig. 6, bottom row**). These WRPs are consistent with the previous findings (**Dawson et al., 2012; Fabiano et al., 2020; Fabiano et al., 2021**).

The OIFS-HRA-15m configuration produces WRPs that are more visually similar to those in ERA-5 than does OIFS-LRA-1h (Fig. 6), a result confirmed by the higher pattern correlation coefficient (PCC) between OIFS-HRA-15m and ERA5 compared to the OIFS-LRA-1h and ERA-5 (**Fig. 6 and 7**). The PCCs for NAO+, NAO- and Sc. Blocking all exceed 0.8 in OIFS-HRA-1h while OIFS-LRA-1h does not achieve PCC above 0.8 for any WRP (**Fig. 6**).

The OIFS-MRA-15m configuration shows smaller PCCs than both the OIFS-HRA-15m and OIFS-LRA-1h configurations (**Fig. 7**), i.e., the improvement from OIFS-LRA-1h to OIFS-HRA-15m does not have a linear relationship with model horizontal resolution or time step. Compared to other configurations and ERA5, OIFS-MRA-15m the z500 anomaly in the NAO+ pattern is too elongated in the southwest-northeast direction, and an unrealistic negative z500 anomaly over the North Atlantic appears in the Sc. Blocking regime (Fig 6). Furthermore, OIFS-MRA-15m shows an Atl. Ridge pattern with neither the right structure nor amplitude.

There is an improvement in the representation of the NAO- regime in the OIFS-LRA-30m configuration over the OIFS-LRA-1h configuration (**Fig. 6**) while the Sc. Blocking regime becomes worse due to the ridge shifting westward. These changes are also reflected in the PCCs (**Fig 7**). Similarly, the OIFS-LRA-15m better represents NAO- and Atl. Ridge than OIFS-LRA-1h while NAO+ and Sc. Blocking worsened. The westward shift of the Sc. Blocking is similar in OIFS-LRA-15m and OIFS-LRA-30m, and the worse NAO+ is related to a northward shift of both the positive and negative z500 anomalies. We note that all experiments use the same SST and sea-ice conditions and that OIFS-LRA-1h, 30m and 15m share the same horizontal resolution, i.e., the changes from OIFS-LRA-1h to OIFS-LRA-15m are not due to SST biases or representation of orography. There does not seem to be a clear improvement as time step is shortened, despite the reduction in mean state biases and Rossby-wave amplitudes and phase speeds.

The PCC is greater than 0.8 for three out of four WRPs in the OIFS-HRA-15m configuration, hence we argue that the OIFS-HRA-15m has the most realistic representation of the weather regimes pattern out of all experiments here. Large improvement in OIFS-HRA-15m over the other configurations could be due to better resolved topography and land-sea contrasts.

### 3.4 Discussion and Conclusions

We have investigated the sensitivity of the climate biases in the OpenIFS atmosphere model to changes in horizontal resolution and time step by analyzing AMIP simulations for the period 1979-2019 (**Table 1**). The strong positive surface zonal wind bias over the Southern Ocean and Northern Hemisphere mid-latitudes and the negative bias in the tropical and subtropical regions have significantly improved in the high horizontal resolution configuration with a short time step (~25km, OIFS-HRA-15m). A similar improvement is observed at the coarse horizontal resolution version with a shorter time step (~100 km with 30 or 15-minutes). The zonal wind bias over the mid-latitudes in both hemispheres is reduced throughout the air column when a smaller time step is used in the coarse resolution version, and we find that the changes in the surface winds are largely due to enhanced shallow and mid-level convection which increases vertical momentum transport. Biases in the surface westerlies in midlatitudes are common in CMIP-class climate models (**Bracegirdle et al., 2020**) and a sensitivity to friction has been noted in idealized model studies (**Chen and Plumb, 2009**). We hypothesize that the enhanced shallow and mid-level convection with a shorter model time step and/or increased horizontal resolution deepened the layer over which friction acts in the lower troposphere so that the frictional effects on the barotropic jet increased, leading to a poleward shift in the jet and reduced biases in zonal wind.

We also find a notable improvement in the representation of the Rossby wave amplitude and phase speed with increased horizontal resolution and shorter time step at least for the waves accounting most variability in both austral and boreal winter seasons. The reduced zonal wind throughout the troposphere with a shorter time step (**Fig. 3**) would decrease the eastward phase speed of Rossby waves, which may explain part of the reduced phase speeds (**Fig. 5**) and reduced biases. However, changes in air-sea interactions or eddy-mean flow interactions may also play a role. In particular, we note that a very large reduction in phase speed biases in austral winter in OIFS-LRA-15m compared to OIFS-LRA-1h were concurrent with very large reduction in zonal surface wind biases.

The weather regime patterns are also more realistic in the high horizontal resolution and short time step configuration OIFS-HRA-15m than OIFS-LRA-1h, but we note that there is no consistent improvement from OIFS-LRA-1h to OIFS-HRA-15m as either horizontal resolution is increased or time step is shortened. For example, both OIFS-MRA-15m and OIFS-LRA-15m are worse than OIFS-LRA-1h. The improvements in the weather regime patterns and Rossby wave amplitude and speed could very well be related to each other as e.g. variations in Rossby wave breaking have been linked to the onset of NAO phases (**Strong and Magnusdottir, 2008**) but this would require further and more targeted analysis. The overall good representation of weather regimes in OIFS-LRA-1h compared to simulations with shorter time steps (OIFS-LRA-30m, OIFS-LRA-15m) may be due to compensation of errors. For example, it is possible that improving the wave amplitudes and phase speeds in OIFS-LRA-30m compared to OIFS-LRA-1h exposes the effect of a biases caused by both the coarse resolution in both configurations, e.g., weak interactions with topography, leading to an overall worse representation of weather regimes.

362   We found a gradual reduction in SAT biases in OpenIFS with increased resolution or shorter time steps. The improvements
363   were largely driven by improvements over North America and eastern Russia. **Roberts et al. (2018)** noted similar SAT biases
364   and linked them to surface albedo, which is thus likely the cause here as well. The improvement with increased resolution
365   and/or shorter time step may be a result of improved snow cover. Systematic improvements in the precipitation biases were
366   not observed. Instead, precipitation biases generally increased with finer horizontal resolution or shorter time step, suggesting
367   that some tuning may be required in the physics parameters when changing horizontal resolution and time step.

368

369   We stress that the results presented in this study are specific to the OpenIFS atmosphere model and are crucial for the modeling
370   community that uses the OpenIFS in their climate models such as EC-Earth (**Haarsma et al., 2020**), CNRM **(Voldoire et al.,**
371   **2019**), AWI (**Streffing et al., 2022**), and GEOMAR **(Kjellsson et al., 2020)**. However, the results may also have implications
372   for other climate modeling communities, at least for those that use a semi-Lagrangian scheme similar to the IFS **(e.g.,Walters**
373   **et al., 2019**) in the atmospheric component where long time steps are both possible and often desirable to reduce the
374   computational cost of the model.

375

376   The zonal wind bias improvement in the OpenIFS is important for research questions linked with the Southern Ocean climate
377   dynamics that plays a crucial role in both the global atmosphere and ocean circulation. We propose that the model time step
378   not be longer than 30 minutes at any horizontal resolution to minimize surface wind biases over the ocean.  The computational
379   cost increases linearly with dt (time step), whereas the cost scales with horizontal resolution as dx^3 as the number of grid
380   points increases in both dimensions and the time step is likely shortened as well. Hence, reducing the model time step from 45
381   or 60 minutes to 20 or 30 minutes may double the computational cost, but lead to significant improvements in the simulated
382   climate. The optimal model time step for the OpenIFS coarse resolution model (1°) is suggested to be 30-minute, but should
383   likely be somewhat shorter, e.g., 15 min, for higher resolutions.

384
385
386
387
388
389
390
391
392

## Code and data availability

The OpenIFS model requires a software license agreement with ECMWF, and OpenIFS' license is easily given free of charge to any academic or research institute. The details of the different versions of the OpenIFS model, including the OpenIFS version used in this study, i.e., 43R3, can be found at https://confluence.ecmwf.int/display/OIFS/About+OpenIFS. The OpenIFS model source code has been made available for the editor and reviewers.

The input datasets (both initial and boundary conditions) needed to run the OpenIFS model, run scripts, the model output, and the Jupiter notebook that support the finding of this study are available at **(Savita, 2023)**. The source code for XIOS 2.5, revision 1910, is available from the official repository at https://forge.ipsl.jussieu.fr/ioserver/ under CeCILL_V2 license. OpenIFS experiments were made using ESM-Tools (https://github.com/esm-tools/esm_tools/). The OASIS coupler is available at https://oasis.cerfacs.fr/en/. The XIOS, ESM-Tools and OASIS coupler used in this study can be downloaded from https://doi.org/10.5281/zenodo.8189718.

The observational datasets used to validate OpenIFS model results in this study are downloaded from the ERA5 (https://cds.climate.copernicus.eu/), GPCP (https://psl.noaa.gov/data/gridded/data.gpcp.html) and CRUTEM4 (http://badc.nerc.ac.uk/data/cru/) websites. Total model output exceeds 10 Tb and it not publicly available, but is available from the authors upon reasonable requests.

## Author contributions

All the model simulations were conducted by AS and JK. Analysis of the output and the writing of text for this paper coordinated by Savita with substantial contributions from JK, RPK, ML, TR, SW and WP.

## Competing interest

The authors declare that they have no conflict of interest.

## Acknowledgement

AS, JK and MK are supported by JPI Climate/Ocean (ROADMAP project grant 01LP2002C). We wish to thank the OpenIFS team at ECMWF for the technical support. All simulations were performed on the HLRN machine under shk00018 project resources. All analyses were performed on computer clusters at GEOMAR and Kiel University Computing Center (NESH). We thanks to Anton Beljaars for discussion on ECMWF model physics.

420  **References**

421  Athanasiadis, P. J., Ogawa, F., Omrani, N.-E., Keenlyside, N., Schiemann, R., Baker, A. J., Vidale, P. L., Bellucci, A.,

422  Ruggieri, P., and Haarsma, R.: Mitigating climate biases in the midlatitude North Atlantic by increasing model resolution: SST

423  gradients and their relation to blocking and the jet, Journal of Climate, 35, 3385-3406, 2022.

424  Bayr, T., Latif, M., Dommenget, D., Wengel, C., Harlaß, J., and Park, W.: Mean-state dependence of ENSO atmospheric

425  feedbacks in climate models, Climate Dynamics, 50, 3171-3194, 2018.

426  Bracegirdle, T., Holmes, C., Hosking, J., Marshall, G., Osman, M., Patterson, M., and Rackow, T.: Improvements in

427  circumpolar Southern Hemisphere extratropical atmospheric circulation in CMIP6 compared to CMIP5, Earth and Space

428  Science, 7, e2019EA001065, 2020.

429  Branković, C. and Gregory, D.: Impact of horizontal resolution on seasonal integrations, Climate Dynamics, 18, 123-143,

430  2001.

431  Chen, G. and Plumb, R. A.: Quantifying the eddy feedback and the persistence of the zonal index in an idealized atmospheric

432  model, Journal of the atmospheric sciences, 66, 3707-3720, 2009.

433  Couldrey, M. P., Gregory, J. M., Boeira Dias, F., Dobrohotoff, P., Domingues, C. M., Garuba, O., Griffies, S. M., Haak, H.,

434  Hu, A., and Ishii, M.: What causes the spread of model projections of ocean dynamic sea-level change in response to

435  greenhouse gas forcing?, Climate Dynamics, 56, 155-187, 2021.

436  Dawson, A., Palmer, T., and Corti, S.: Simulating regime structures in weather and climate prediction models, Geophysical

437  Research Letters, 39, 2012.

438  Eyring, V., Bony, S., Meehl, G. A., Senior, C. A., Stevens, B., Stouffer, R. J., and Taylor, K. E.: Overview of the Coupled

439  Model Intercomparison Project Phase 6 (CMIP6) experimental design and organization, Geoscientific Model Development,

440  9, 1937-1958, 2016.

441  Fabiano, F., Meccia, V. L., Davini, P., Ghinassi, P., and Corti, S.: A regime view of future atmospheric circulation changes in

442  northern mid-latitudes, Weather and Climate Dynamics, 2, 163-180, 2021.

443  Fabiano, F., Christensen, H., Strommen, K., Athanasiadis, P., Baker, A., Schiemann, R., and Corti, S.: Euro-Atlantic weather

444  Regimes in the PRIMAVERA coupled climate simulations: impact of resolution and mean state biases on model performance,

445  Climate Dynamics, 54, 5031-5048, 2020.

446 Flato, G., Marotzke, J., Abiodun, B., Braconnot, P., Chou, S. C., Collins, W., Cox, P., Driouech, F., Emori, S., and Eyring, V.:

447 Evaluation of climate models, in: Climate change 2013: the physical science basis. Contribution of Working Group I to the

448 Fifth Assessment Report of the Intergovernmental Panel on Climate Change, Cambridge University Press, 741-866, 2014.

449 Forbes, R. and Tompkins, A.: An improved representation of cloud and precipitation, ECMWF Newsletter, 129, 13-18, 2011.

450 Gates, W. L., Boyle, J. S., Covey, C., Dease, C. G., Doutriaux, C. M., Drach, R. S., Fiorino, M., Gleckler, P. J., Hnilo, J. J.,

451 and Marlais, S. M.: An overview of the results of the Atmospheric Model Intercomparison Project (AMIP I), Bulletin of the

452 American Meteorological Society, 80, 29-56, 1999.

453 Gelaro, R., McCarty, W., Suárez, M. J., Todling, R., Molod, A., Takacs, L., Randles, C. A., Darmenov, A., Bosilovich, M. G.,

454 and Reichle, R.: The modern-era retrospective analysis for research and applications, version 2 (MERRA-2), Journal of

455 climate, 30, 5419-5454, 2017.

456 Haarsma, R., Acosta, M., Bakhshi, R., Bretonnière, P.-A. B., Caron, L.-P., Castrillo, M., Corti, S., Davini, P., Exarchou, E.,

457 and Fabiano, F.: HighResMIP versions of EC-Earth: EC-Earth3P and EC-Earth3P-HR. Description, model performance, data

458 handling and validation, (No Title), 2020.

459 Harris, I., Jones, P. D., Osborn, T. J., and Lister, D. H.: Updated high-resolution grids of monthly climatic observations–the

460 CRU TS3. 10 Dataset, International journal of climatology, 34, 623-642, 2014.

461 Hazeleger, W., Wang, X., and Severijns, C.: SS tef anescu, R Bintanja, A Sterl, Klaus Wyser, T Semmler, S Yang, B Van den

462 Hurk, et al. Ec-earth v2. 2: description and validation of a new seamless earth system prediction model, Climate dynamics, 39,

463 2611-2629, 2012.

464 He, C. and Zhou, T.: The two interannual variability modes of the western North Pacific subtropical high simulated by 28

465 CMIP5–AMIP models, Climate dynamics, 43, 2455-2469, 2014.

466 Hersbach, H., Bell, B., Berrisford, P., Hirahara, S., Horányi, A., Muñoz-Sabater, J., Nicolas, J., Peubey, C., Radu, R., and

467 Schepers, D.: The ERA5 global reanalysis, Quarterly Journal of the Royal Meteorological Society, 146, 1999-2049, 2020.

468 Hogan, R. J. and Bozzo, A.: A flexible and efficient radiation scheme for the ECMWF model, Journal of Advances in Modeling

469 Earth Systems, 10, 1990-2008, 2018.

470 Huffman, G. J., Adler, R. F., Arkin, P., Chang, A., Ferraro, R., Gruber, A., Janowiak, J., McNab, A., Rudolf, B., and Schneider,

471 U.: The global precipitation climatology project (GPCP) combined precipitation dataset, Bulletin of the american

472 meteorological society, 78, 5-20, 1997.

473    Jung, T., Miller, M., Palmer, T., Towers, P., Wedi, N., Achuthavarier, D., Adams, J., Altshuler, E., Cash, B., and Kinter Iii, J.:

474    High-resolution global climate simulations with the ECMWF model in Project Athena: Experimental design, model climate,

475    and seasonal forecast skill, Journal of Climate, 25, 3155-3172, 2012.

476    Kim, S. T., Cai, W., Jin, F.-F., and Yu, J.-Y.: ENSO stability in coupled climate models and its association with mean state,

477    Climate dynamics, 42, 3313-3321, 2014.

478    Kjellsson, J., Streffing, J., Carver, G., and Köhler, M.: From weather forecasting to climate modelling using OpenIFS, ECMWF

479    Newsletter, 164, 38-41, 2020.

480    Liu, B., Gan, B., Cai, W., Wu, L., Geng, T., Wang, H., Wang, S., Jing, Z., and Jia, F.: Will increasing climate model resolution

481    be beneficial for ENSO simulation?, Geophysical Research Letters, 49, e2021GL096932, 2022.

482    Ma, P.-L., Harrop, B. E., Larson, V. E., Neale, R. B., Gettelman, A., Morrison, H., Wang, H., Zhang, K., Klein, S. A., and

483    Zelinka, M. D.: Better calibration of cloud parameterizations and subgrid effects increases the fidelity of the E3SM Atmosphere

484    Model version 1, Geoscientific Model Development, 15, 2881-2916, 2022.

485    Meehl, G. A. and Teng, H.: CMIP5 multi-model hindcasts for the mid-1970s shift and early 2000s hiatus and predictions for

486    2016–2035, Geophysical Research Letters, 41, 1711-1716, 2014.

487    Meng, Y., Hao, Z., Feng, S., Guo, Q., and Zhang, Y.: Multivariate bias corrections of CMIP6 model simulations of compound

488    dry and hot events across China, Environmental Research Letters, 17, 104005, 2022.

489    Osborn, T. and Jones, P.: The CRUTEM4 land-surface air temperature data set: construction, previous versions and

490    dissemination via Google Earth, Earth System Science Data, 6, 61-68, 2014.

491    Pilch Kedzierski, R., Matthes, K., and Bumke, K.: New insights into Rossby wave packet properties in the extratropical UTLS

492    using GNSS radio occultations, Atmospheric Chemistry and Physics, 20, 11569-11592, 2020.

493    Roberts, C. D., Senan, R., Molteni, F., Boussetta, S., Mayer, M., and Keeley, S. P.: Climate model configurations of the

494    ECMWF Integrated Forecasting System (ECMWF-IFS cycle 43r1) for HighResMIP, Geoscientific model development, 11,

495    3681-3712, 2018.

496    Savita, A.: Assessment of Climate Biases in OpenIFS Version 43R3 across Model Horizontal Resolutions and Time Steps

497    [dataset], https://hdl.handle.net/20.500.12085/c74887dc-e609-4392-9faf-48c67276d5d1, 2023.

498  Simmons, A. J. and Burridge, D. M.: An energy and angular-momentum conserving vertical finite-difference scheme and

499  hybrid vertical coordinates, Monthly Weather Review, 109, 758-766, 1981.

500  Streffing, J., Sidorenko, D., Semmler, T., Zampieri, L., Scholz, P., Andrés-Martínez, M., Koldunov, N., Rackow, T., Kjellsson,

501  J., and Goessling, H.: AWI-CM3 coupled climate model: description and evaluation experiments for a prototype post-CMIP6

502  model, Geoscientific Model Development, 15, 6399-6427, 2022.

503  Strong, C. and Magnusdottir, G.: Tropospheric Rossby wave breaking and the NAO/NAM, Journal of the atmospheric

504  sciences, 65, 2861-2876, 2008.

505  Taylor, K. E., Stouffer, R. J., and Meehl, G. A.: An overview of CMIP5 and the experiment design, Bulletin of the American

506  meteorological Society, 93, 485-498, 2012.

507  Temperton, C., Hortal, M., and Simmons, A.: A two-time-level semi-Lagrangian global spectral model, Quarterly Journal of

508  the Royal Meteorological Society, 127, 111-127, 2001.

509  Tiedtke, M.: Representation of clouds in large-scale models, Monthly Weather Review, 121, 3040-3061, 1993.

510  Van Noije, T., Bergman, T., Le Sager, P., O'Donnell, D., Makkonen, R., Gonçalves-Ageitos, M., Döscher, R., Fladrich, U.,

511  Von Hardenberg, J., and Keskinen, J.-P.: EC-Earth3-AerChem: a global climate model with interactive aerosols and

512  atmospheric chemistry participating in CMIP6, Geoscientific Model Development, 14, 5637-5668, 2021.

513  Voldoire, A., Saint-Martin, D., Sénési, S., Decharme, B., Alias, A., Chevallier, M., Colin, J., Guérémy, J. F., Michou, M., and

514  Moine, M. P.: Evaluation of CMIP6 deck experiments with CNRM-CM6-1, Journal of Advances in Modeling Earth Systems,

515  11, 2177-2213, 2019.

516  Walters, D., Baran, A. J., Boutle, I., Brooks, M., Earnshaw, P., Edwards, J., Furtado, K., Hill, P., Lock, A., and Manners, J.:

517  The Met Office Unified Model global atmosphere 7.0/7.1 and JULES global land 7.0 configurations, Geoscientific Model

518  Development, 12, 1909-1963, 2019.

519  Williamson, D. L., Kiehl, J. T., and Hack, J. J.: Climate sensitivity of the NCAR Community Climate Model (CCM2) to

520  horizontal resolution, Climate Dynamics, 11, 377-397, 1995.

521  Wolf, G. and Wirth, V.: Diagnosing the horizontal propagation of Rossby wave packets along the midlatitude waveguide,

522  Monthly Weather Review, 145, 3247-3264, 2017.

523 Zhou, S., Huang, G., and Huang, P.: Excessive ITCZ but negative SST biases in the tropical Pacific simulated by CMIP5/6

524 models: The role of the meridional pattern of SST bias, Journal of Climate, 33, 5305-5316, 2020.

525 **Table**

526

| Experiment Name | Horizontal resolution | Vertical grid | Time step |
|---|---|---|---|
| **OIFS-LRA-15m** | Tco95/100km | L91 | 15m |
| **OIFS-MRA-15m** | Tco199/50km | L91 | 15m |
| **OIFS-HRA-15m** | Tco399/25km | L91 | 15m |
| **OIFS-LRA-30m** | Tco95/100km | L91 | 30m |
| **OIFS-LRA-1h** | Tco95/100km | L91 | 1h |

527

528 **Table 1**. List of the experiments performed across different horizontal resolutions and model time steps using OIFS model.

529

530

531
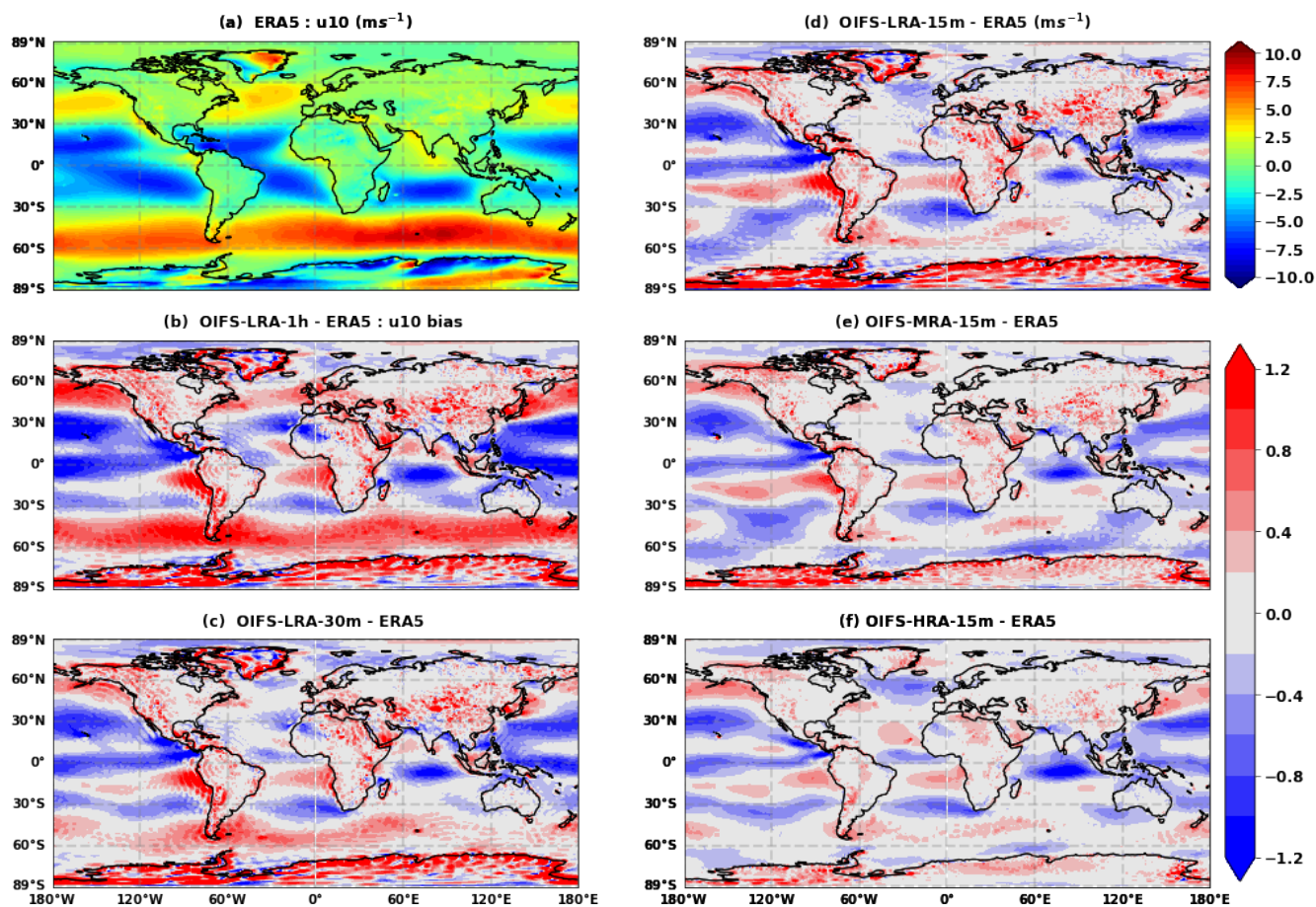
**Figures**

**Figure 1**. (a) Annual mean ERA5 surface zonal wind [ms⁻¹]. (b-d) Annual mean zonal wind [ms⁻¹] bias for different model time steps (1h (b), 30m (c), and 15m (d)) using ~100 km resolution, and (e-f) with different horizontal resolutions, ~50 (e) and ~25 km (f), respectively. Biases are computed with respect to ERA5 over the period 1979–2019.

**(a) Root Mean Square Error**

**(b)**

**(c)**

538
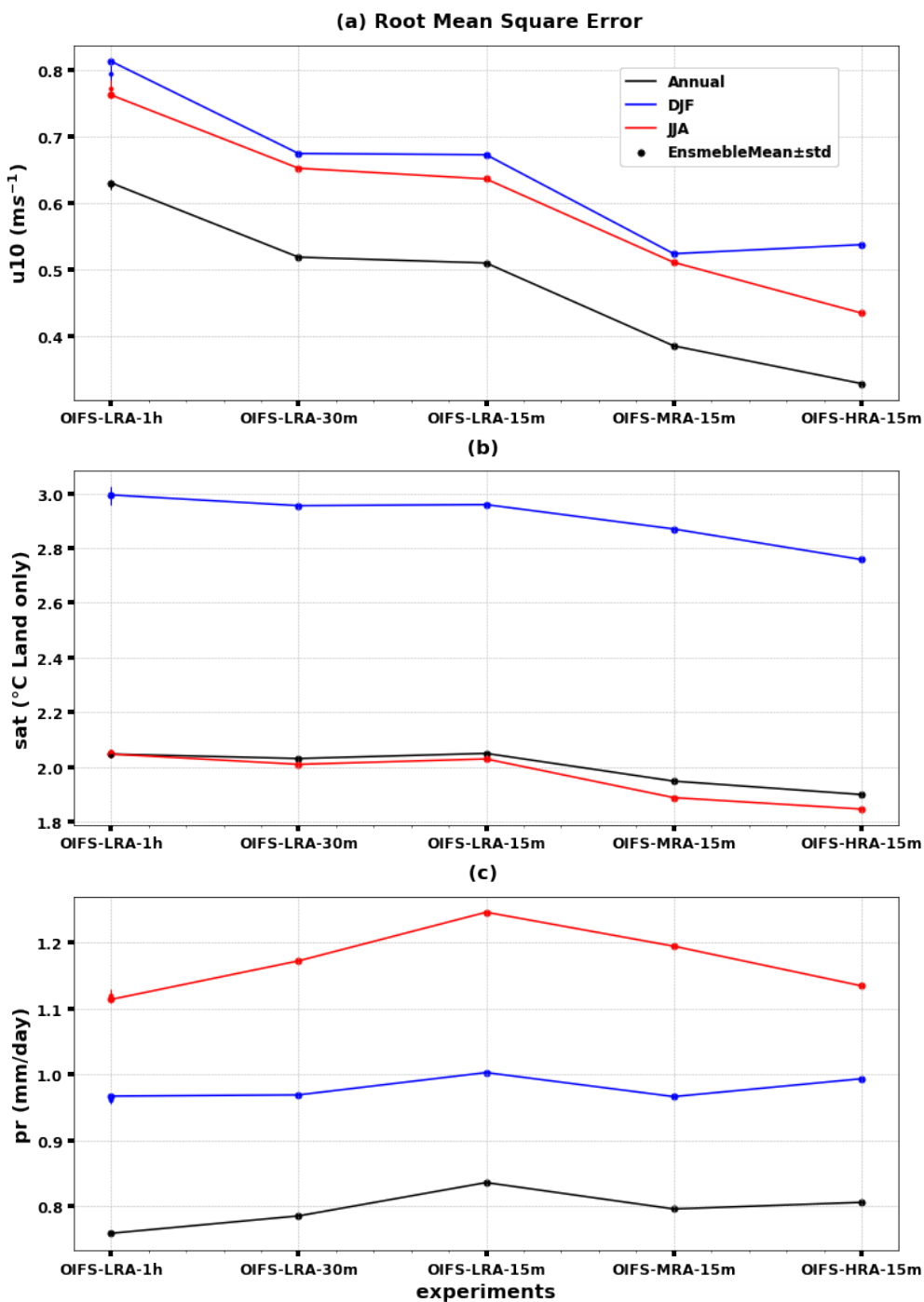
**Figure 2**. Root mean squared error of surface zonal wind (a), SAT (b), and precipitation (c) over the period 1979-2019 for all
the configurations: annual (black) and seasonal mean (DJF: blue, JJA: red). We have also shown 5-member ensemble mean
and standard deviation only for OIFS-LRA-1h configuration.

542
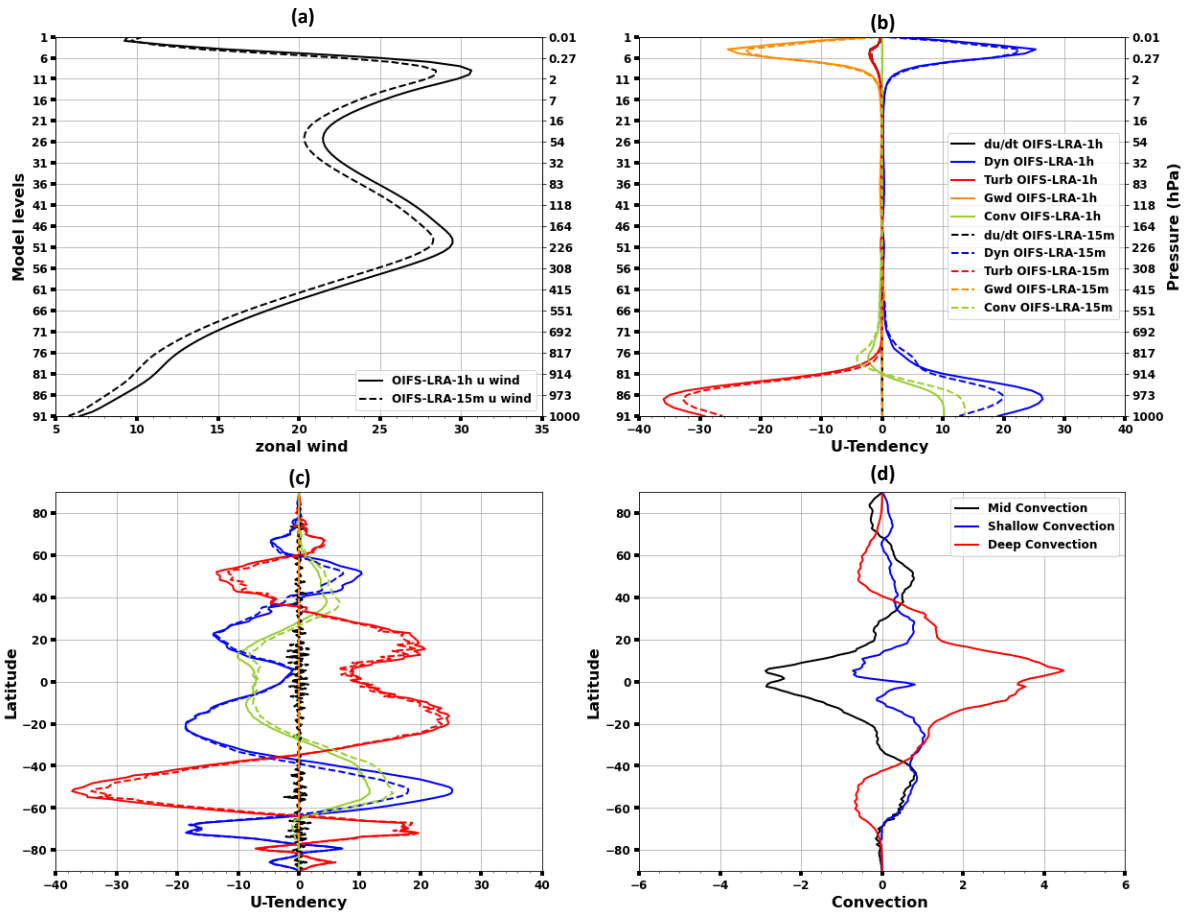
543

544

545 **Figure 3**. (a) Averaged zonal wind (u) [ms$^{-1}$] and zonal wind tendencies [ms$^{-2}$/hour] over the Southern Ocean (40°S – 60°S,

546 all longitude) as a function of height for OIFS-LRA-1h and OIFS-LRA-15m. Model levels (y-axis left) and pressure levels (y-

547 axis right). (c) Zonal and time average of zonal wind tendencies at the lowest level of the model as a function of latitude. (d)

548 Zonal and time average convection difference [Kgm$^{-2}$/hour] between OIFS-LRA -15m and OIFS-LRA-1h configurations. The

549 solid lines in panels (b) and (c) show the wind tendency for OIFS-LRA-1h configuration whereas the dashed lines are for

550 OIFS-LRA-15m configuration. Shown are averages over 1979-2019.

551
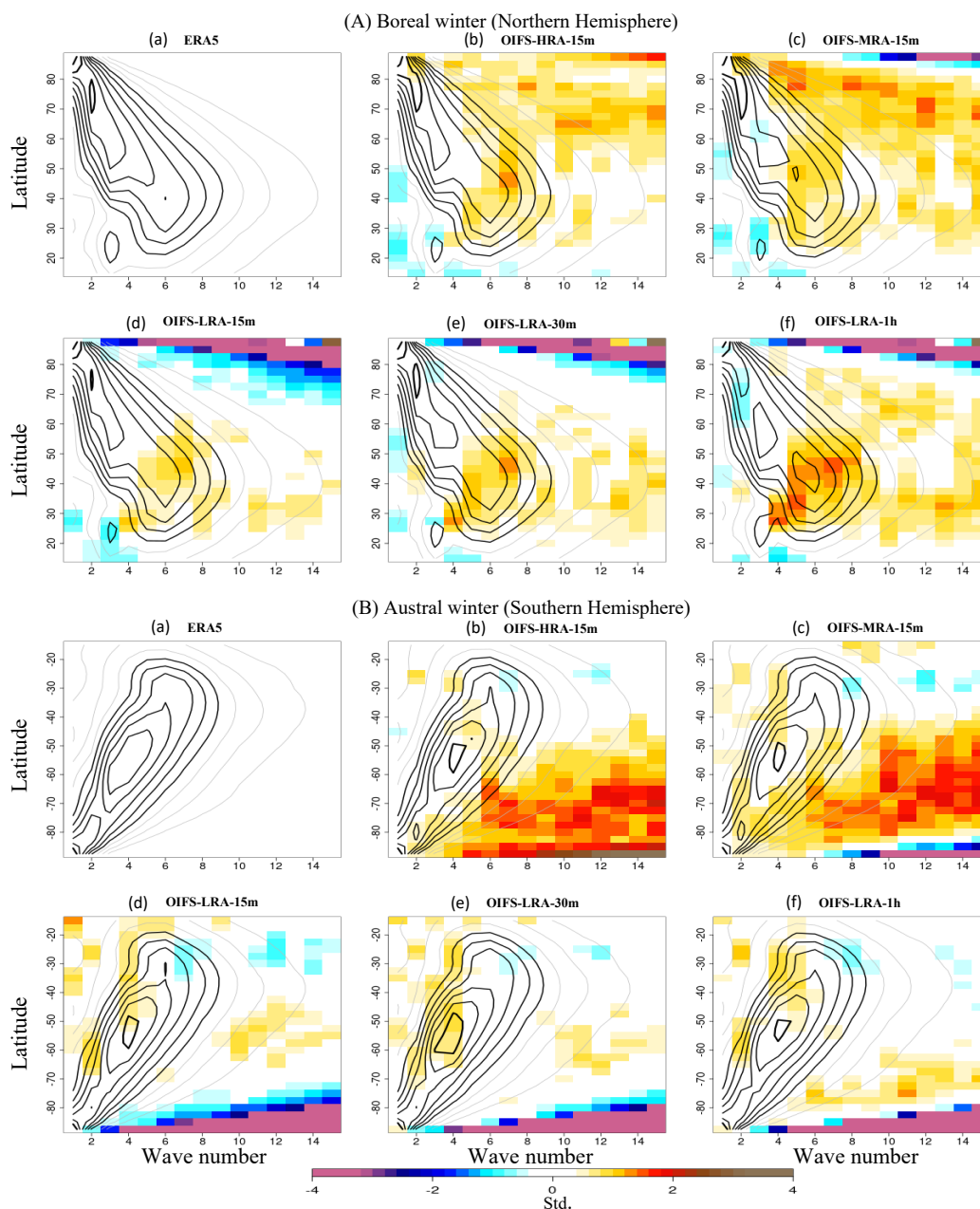
**Figure 4**. (A) The Rossby wave amplitude (contours) for different wave numbers in the Northern Hemisphere at 300 hPa (a) in ERA5 observation and (b-f) in the OIFS model simulations during 1979-2019 in DJF (i.e., boreal winter). The color shows the detrended and standardized difference of wave amplitude between the model and ERA5 where it is significant on the 95 % confidence level. The wave amplitude and contour interval are shown in ms$^{-1}$. The grey contours start from 2 ms$^{-1}$ and the black contours from 5 ms$^{-1}$ and the contour interval is 1 ms$^{-1}$. (B) is similar to (A), but for JJA (i.e., austral winter).

(A) Boreal winter (Northern Hemisphere)

(a) ERA5     (b) OIFS-HRA-15m     (c) OIFS-MRA-15m

(d) OIFS-LRA-15m     (e) OIFS-LRA-30m     (f) OIFS-LRA-1h

(B) Austral winter (Southern Hemisphere)

(a) ERA5     (b) OIFS-HRA-15m     (c) OIFS-MRA-15m

(d) OIFS-LRA-15m     (e) OIFS-LRA-30m     (f) OIFS-LRA-1h
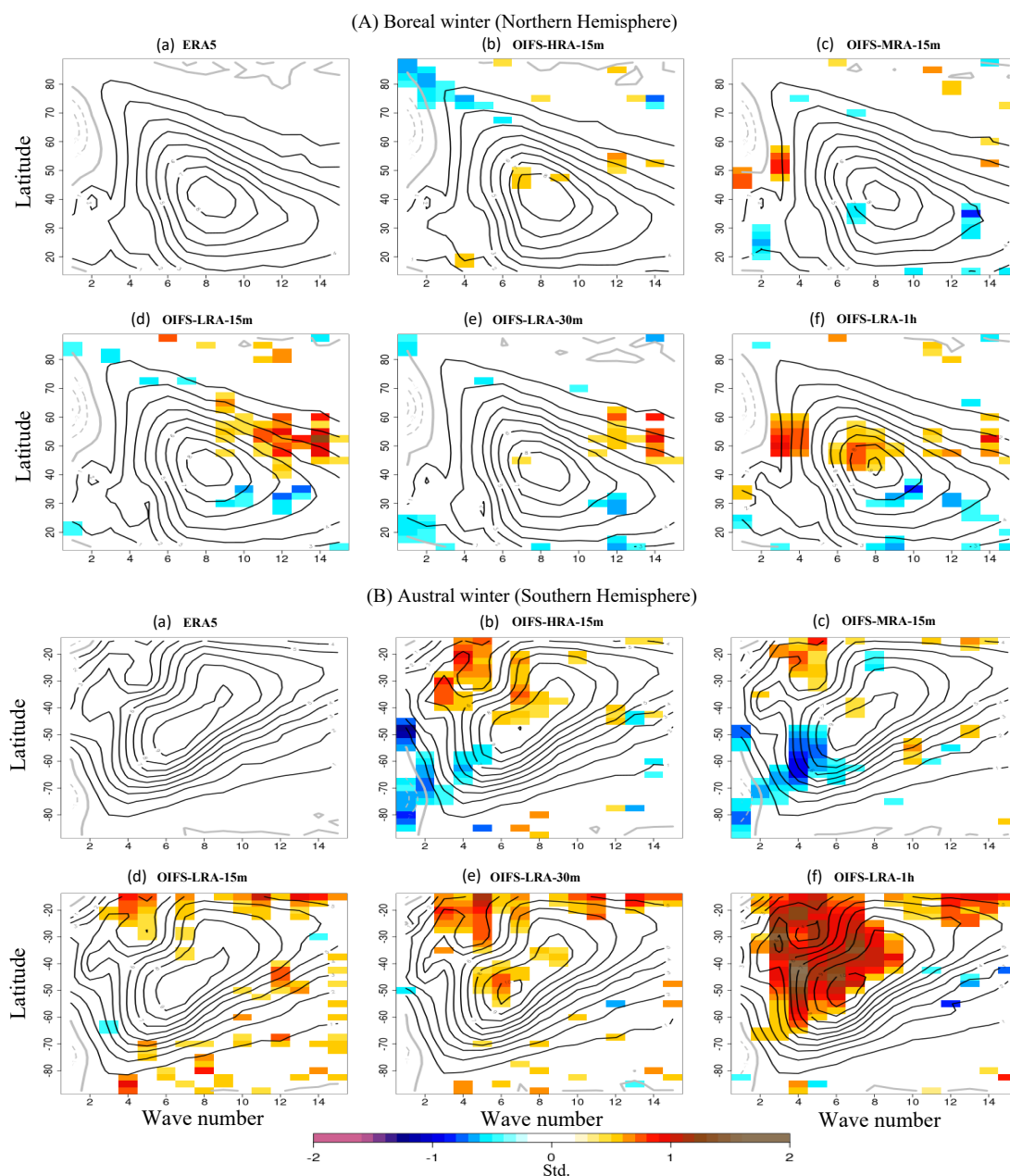
**Figure 5.** (A) The Rossby wave phase speed (contours) for different wave numbers at 300 hPa in the Northern Hemisphere in ERA5 (a) observation and (b-f) in the OIFS model simulations during 1979-2019 in DJF (i.e., boreal winter). The color shows the detrended and standardized difference of wave phase speed between model and ERA5 where it is significant on the 95 % confidence level. The wave phase speed and contour interval are shown in ms$^{-1}$. The contours start from 1 ms$^{-1}$ and the contour interval is 1 ms$^{-1}$. Panel (B) is similar to panel (A), but for JJA (i.e., austral winter).
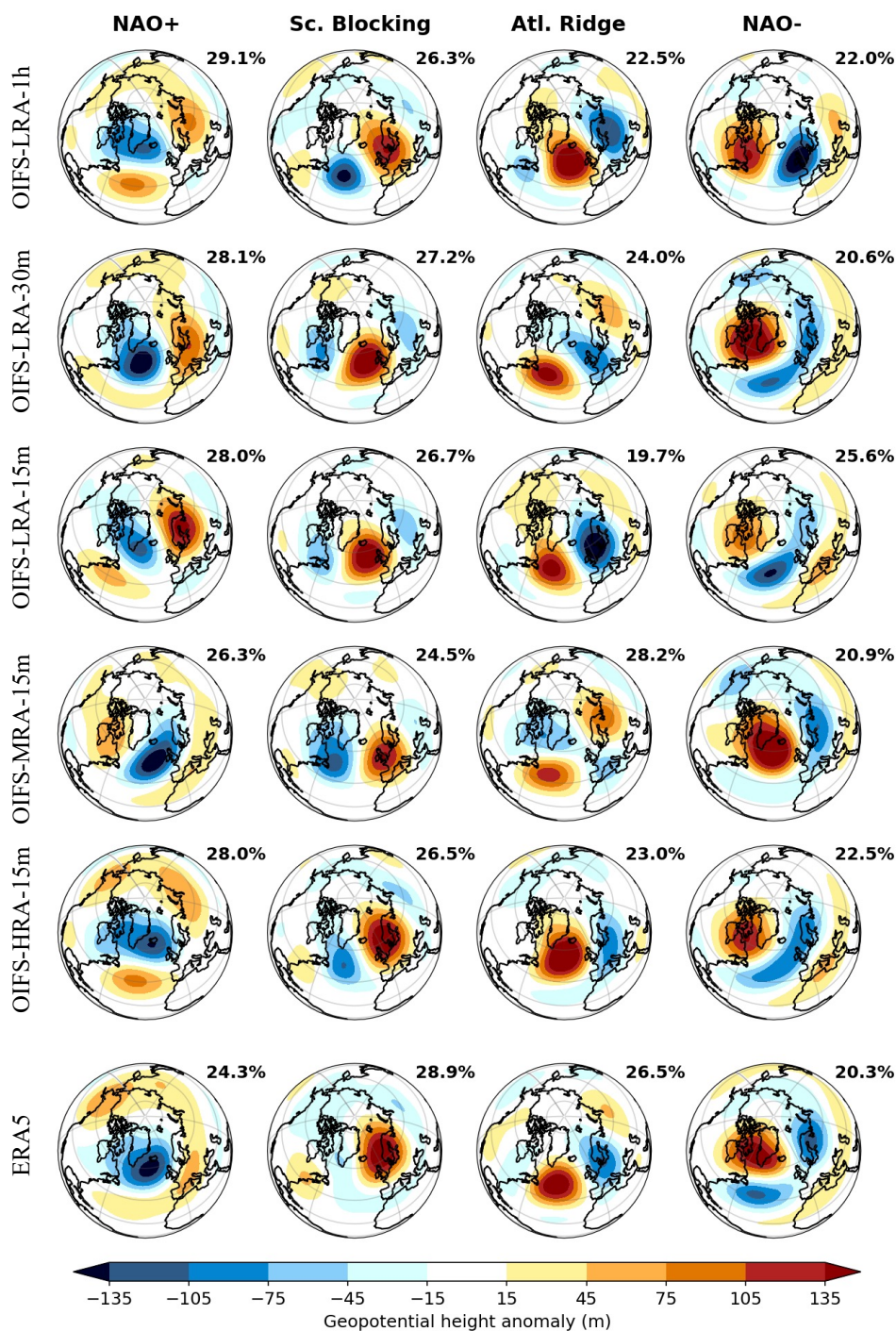
**Figure. 6.** Weather regime patterns over the Euro–Atlantic regions from ERA5 observation (bottom row) and the individual OIFS model simulations (1st to 5th row) over the time period 1979–2019 for DJF (boreal winter season).

568

569
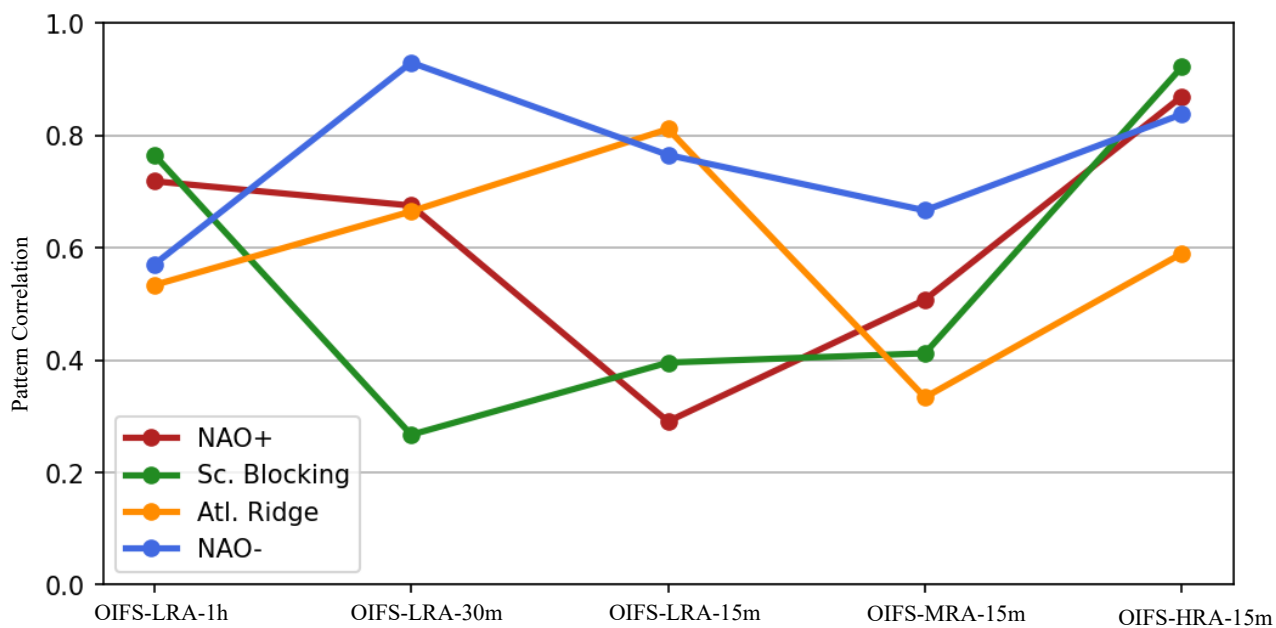
**Figure. 7.** Pattern correlation coefficient of the individual weather regime between OIFS model configurations and ERA5 for the period 1979-2019 for the DJF season.

572

573

574